Journal of Physics and Chemistry of Solids 149 (2021) 109790

Contents lists available at ScienceDirect

Journal of Physics and Chemistry of Solids

journal homepage: http://www.elsevier.com/locate/jpcs

Presence of excited electronic states on terbium incorporation in $CaMoO_4$: Insights from experimental synthesis and first-principles calculations

Ricardo L. Tranquilin [a,c], Marisa C. Oliveira [a,*], Anderson A.G. Santiago [a], Laura X. Lovisa [a], Renan A.P. Ribeiro [b], Elson Longo [c], Sergio R. de Lazaro [d], Cláudio R.R. Almeida [a], Carlos A. Paskocimas [a], Fabiana V. Motta [a], Mauricio R.D. Bomio [a]

[a] Laboratory of Chemical Synthesis of Materials, Department of Materials Engineering, Federal University of Rio Grande do Norte, P.O. Box 1524, Natal, RN, 59078-900, Brazil
[b] Department of Chemistry, State University of Minas Gerais, Av. Paraná, 3001, Divinópolis, MG, 35501-170, Brazil
[c] CDMF-LIEC, Federal University of São Carlos, P.O. Box 676, São Carlos – SP, 13565-905, Brazil
[d] Department of Chemistry, State University of Ponta Grossa, Av. General Carlos Cavalcanti, P.O. Box 4748, Ponta Grossa, PR, 84030-900, Brazil

ARTICLE INFO

Keywords:
$CaMoO_4$
Density functional theory
Terbium
Photoluminescence
Ultrasonic spray pyrolysis

ABSTRACT

We present a combined experimental and theoretical study to understand the structure and electronic and optical properties of CaMoO4:*x*Tb3+ ($x = 1$ mol%, 2 mol%, and 4 mol%) microspheres. The microspheres were prepared by ultrasonic spray pyrolysis and characterized by X-ray diffraction (XRD), field-emission gun scanning electron microscopy (FEG-SEM), micro Raman spectroscopy, and photoluminescence (PL) spectroscopy. First-principles quantum mechanical calculations were performed at the density functional theory level to obtain the geometry and electronic properties of $CaMoO_4$:*x*Tb^{3+} microspheres in the ground electronic state and excited electronic states (singlet and triplet). These results, combined with XRD patterns, indicate that these crystals have a scheelite-type tetragonal structure. The morphology of the $CaMoO_4$:*x*Tb3+($x = 1$ mol%, 2 mol%, and 4 mol%) samples was investigated by FEG-SEM, and a spherical shape was found. The optical properties were investigated by UV–vis spectroscopy and PL spectroscopy, and the chromaticity coordinates of these compounds were obtained. The relationships between the PL properties and the Raman spectra indicate that Tb3+-doped CaMoO4 microspheres constitute promising photoluminescent materials for use in new lighting devices. This also allowed us to understand the charge transfer process that happens in the singlet (s) ground state and the singlet (s*) and triplet (t*) excited states, which generates the photoluminescent emissions of the Tb^{3+}-doped $CaMoO_4$ microspheres.

1. Introduction

Many investigations in recent decades have focused on the luminescence properties of rare-earth ion–doped scheelite-type oxides, such as $CaMoO_4$ (Pr, Yb, Eu, Dy) [1–4], $CaWO_4$ and $CdMoO_4$ (Tb) [5,6], $SrMoO_4$ (Eu) [7], $PbMoO_4$ (Eu, Tb, Tm) [8], and $BaMoO_4$ (Er, Eu) [9,10], because of their stability under extreme environmental conditions and because they could constitute an outstanding property for the application of such oxides. Thus, a number of scheelite compounds with the chemical formula ABO_4 [11] (where A = Ca, Sr, Ba, or Pb, and B = Mo), and in particular calcium molybdate ($CaMoO_4$), with tetragonal structure and space group $I4_1/a$ [12] can be used for numerous technological applications, especially for electronic optics [1,2,13,14].

$CaMoO_4$ has been a promising candidate in this field in recent years because of its structural versatility and stability. It has attracted the interest of many researchers because of its broad potential in applications, including mainly luminescence, scintillation [15–22], and photocatalysis [23], because of its ability to display a wide range of physical and chemical properties depending on the metal occupancies of the A and B sites.

Furthermore, several experimental studies have been used to improve the photoluminescence (PL) properties of the $CaMoO_4$ matrix by a rare-earth doping mechanism as reported for Tb^{3+}-doped $CaMoO_4$ ($CaMoO_4$:Tb^{3+}) samples with use of different techniques such as the flux growth method, the precipitation method, and microwave-assisted ionic liquid–based synthesis [5,20,24–26]. In contrast, the ultrasonic spray

* Corresponding author.
E-mail address: marisa-coliveira@hotmail.com (M.C. Oliveira).

https://doi.org/10.1016/j.jpcs.2020.109790
Received 18 April 2020; Received in revised form 26 September 2020; Accepted 28 September 2020
Available online 2 October 2020

pyrolysis (USP) method has some advantages over these methods in the production of oxides, such as simple equipment with easy control of the experimental parameters, precursor solution prepared by metallic nitrates dissolved in water, and rapid production of spherical particles in one step with high purity and homogeneity, but high temperatures are needed compared with hydrothermal methods [27,28].

A detailed understanding of the excited states involved in optical phenomena such as photoluminescent emission is a challenging task [29,30]; consequently, one has to resort to quantum chemical simulations to provide a better understanding of experimental results in order to help ascertain the geometry and electronic structure of the excited electronic states and therefore prediction of the PL behavior. In this approach, numerous efforts by our research group have been made to understand the mechanism of photoluminescent emission. This computational technique has been successfully used for the study of the electronic and structural properties of several materials, such as $Ca_{10}V_6O_{25}$ [31], $CaZrO_3$ [32], $CaZrO_3$:Eu [33], $SrTiO_3$ [34], $SrTiO_3$:Sm [35], $CaWO_4$ [36], $BaZrO_3$ [37], and Ag_2O [38], on the basis of the characterization of excited electronic states.

In this work, an effort has been made in that direction and, for the first time, first-principles calculations on the presence of excited electronic states are used to complement the experimental evaluation of PL of $CaMoO_4$:xTb^{3+} (x = 1 mol%, 2 mol% and 4 mol%) microspheres obtained by the USP method. $CaMoO_4$:Tb^{3+} is an attractive material for optical applications because it shows characteristic Tb^{3+}-related strong green emission ($^5D_4 \rightarrow {}^7F_5$, ~545.5 nm). Herein, the characteristics and influence of the Tb^{3+} ions are discussed in terms of X-ray diffraction (XRD), Raman spectroscopy, PL measurements, chromaticity coordinates, and field-emission gun scanning electron microscopy (FEG-SEM). Furthermore, the localization and characterization of the excited singlet and triplet electronic states allowed us to rationalize the photoluminescent emissions of this material.

2. Experimental

2.1. Materials

Molybdic acid (H_2MoO_4, 85%, Alfa Aesar), calcium nitrate ($Ca(NO_3)_2{\cdot}4H_2O$, 99%, Alfa Aesar), terbium nitrate pentahydrate ($Tb(NO_3){\cdot}5H_2O$, 99.9%, Aldrich), and distilled water were used as received to prepare the $CaMoO_4$:xTb3+(x = 1 mol%, 2 mol%, and 4 mol%) microspheres.

2.2. Preparation of CaMoO4:xTb3+(x = 1 mol%, 2 mol%, and 4 mol%) microspheres

As previously reported by Almeida et al. [39], the pure $CaMoO_4$ microspheres, and in this work, $CaMoO_4$ doped with Tb^{3+} ions were obtained by the USP method. To prepare $CaMoO_4$:xTb^{3+}, the precursor solution was prepared by our dissolving 0.045 mol of $Ca(NO_3)_2{\cdot}4H_2O$ and 0.09 mol of H_2MoO_4 in 100 mL of distilled water. This precursor solution was then transferred to a beaker and was then kept under constant stirring at a temperature of approximately 60 °C. Next, 1 mol%, 2 mol%, and 4 mol% Tb^{3+} (prepared though the dissolution of $Tb(NO_3){\cdot}5H_2O$) were stoichiometrically added to this reaction mixture under constant stirring and a stabilized temperature (60 °C) for approximately 30 min.

The precursor solution was atomized with an ultrasonic nebulizer (frequency of 2.4 MHz) with an airflow of 2 L min^{-1} and heated by an electric furnace at 1000 °C in air. More details on the equipment and technique used are given in Ref. [39].

The USP method was successfully used for the synthesis of various systems, such as Ca-doped $SrIn_2O_4$ [40], Sr0.9−x−y−zCa0.1In2O4:(xEu3+, yTm3+, zTb3+) [41], $Li_2Ti_3O_7$ [42], gold nanoparticles [43], TiO2 [44], and $Ba_{1-x}Zn_xMoO_4$ [45].

2.3. Characterization of CaMoO4:xTb3+ microspheres

XRD patterns of the samples were measured with a Shimadzu XRD-7000 X-ray diffractometer with Cu Kα radiation (λ = 1.5406 Å) in the 2θ range from 10° to 80° at a scan rate of 0.02 s^{-1}. For the Rietveld refinement measurements, a 2θ range from 10° to 80° and a step size of 0.02° min^{-1} were used, and the General Structure Analysis System (GSAS) program with the EXPGUI graphical interface was used to perform the refinement. Micro Raman spectroscopy measurements were conducted with a T64000 spectrometer (Horiba Jobin Yvon, France) with a triple monochromator coupled to a charge-coupled detector. The spectra were obtained with use of the 514.5 nm wavelength of an argon-ion laser, with its maximum output power kept at 8 mW. The morphologies of the samples were observed by FEG-SEM with a Supra 35 VP instrument (Carl Zeiss, Germany) operated at 6 kV. The PL spectra were obtained with an Monospec 27 monochromator (Thermal Jarrell Ash, USA) and an R446 photomultiplier (Hamamatsu Photonics, USA). The 350 nm beam of a krypton ion laser (Coherent Innova 90 K) was used as the excitation source with a maximum output power of 200 mW. UV–vis spectra were recorded with a UV-2600 spectrophotometer (Shimadzu) in reflectance mode. All measurements were performed at room temperature.

3. Computational methods

Calculations were performed with the periodic ab initio CRYSTAL17 package [46] on the basis of density functional theory with the hybrid functional of a nonlocal exchange functional developed from Becke combined with a correlation functional based on the gradient of electronic density developed by Lee, Yang, and Parr (B3LYP) [47,48]. This computational technique has been successfully applied for the study of the electronic and structural properties of various materials, including zirconates, vanadates, and several other oxides [31–33].

The atomic centers were described with use of standard all-electron basis sets for the O (O_6-31d1_gatti_1994) [49] and Ca (Ca_86-511d3G_catti_1991) [50] atoms, whereas the Mo (Mo_SC_HAYWSC-311(d31)G_cora_1997) [51] and Tb (Tb_ERD_SMALL_CORE_PP_4F_IN_VALENCE_NO_G_2017) atoms were described by pseudopotential basis sets. In particular, for Tb^{3+} ions, we used basis sets with the format CP28MWB-(11s11p7d8f)/[4s4p2d3f], where the valence was described by four sp shells, 2 d shells, and three f shells [52]. The accuracy of the evaluation of the Coulomb and exchange series was controlled by five thresholds with values of 10^{-6}, 10^{-6}, 10^{-6}, 10^{-6}, and 10^{-12}. Regarding the density matrix diagonalization, the reciprocal space net was described by a shrinking factor set to 4, corresponding to 36 k-points within the irreducible part of the Brillouin zone in accordance with the Monkhorst-Pack method [53].

The calculation of the equilibrium geometries and electronic properties of the $CaMoO_4$:Tb^{3+} (12.5% doping) system was used to simulate the tetragonal supercell structure of 95 atoms, which corresponds to 2 × 2 × 2 conventional cells in which two Ca^{2+} cations were replaced by two Tb^{3+} cations and a calcium vacancy was created to neutralize the unit cell. For the calculation of the doped materials ($CaMoO_4$:Tb^{3+}), the experimental doping percentages were 1 mol%, 2 mol%, and 4 mol% as it was necessary to use very large unit cells. The calculations were therefore computationally complex, and a minimum doping amount of 12.5% could be achieved separately for the Tb^{3+} cations.

To understand the PL mechanism associated with the Tb^{3+} doping process in $CaMoO_4$, the excited singlet state (s*) and the excited triplet state (t*) were both localized and characterized, following the previous strategies developed by our group [31–33]. For the s* model, we consider an off-center Ca displacement of 0.1 Å in the z direction. In this case, the t* model state was reproduced by our fixing the difference between spin-up (α) and spin-down (β) configurations ($n\alpha - n\beta = 2$) during the self-consistent field calculations. The electronic structure was investigated by means of the band structure, the density of states (DOS),

and the spin density isosurfaces.

4. Results and discussion

4.1. XRD, FEG-SEM, and Raman analysis

We recently reported XRD patterns of pure $CaMoO_4$ powders prepared under favorable conditions by the USP method at 600 °C and 1000 °C [39]. The peaks become more intense with the increase in temperature, indicating that the increase in temperature results in better crystallization, and therefore we used 1000 °C for the subsequent characterizations.

Fig. 1 shows XRD patterns of $CaMoO_4$:$x$$Tb^{3+}$ samples synthesized by USP at 1000 °C; the patterns show there was no secondary phase formation. The position and intensity of the diffraction peaks of these samples are consistent with those of standard powder diffraction files (ICSD 60552) and can be indexed in a scheelite-type tetragonal structure with space group $I4_1/a$ and point group symmetry $4/m$.

Fig. 1b shows the effect of replacement of Ca^{2+} by Tb^{3+} for $x = 1$ mol %, 2 mol%, and 4 mol%. In all powders, the strongest peak at around $2\theta = 28°$ corresponds to the (112) crystalline plane; however, doping with Tb^{3+} cations changes the lattice because of the distinct electronic density with respect to Ca^{2+} ions and the introduction structural defects with the formation of [TbO_8] clusters and calcium vacancies [39]. In addition, the samples with 2 mol% and, especially, 4 mol% doping showed extra peaks at 2θ of 12.87°, 25.71°, 32.02°, 33.52°, and 36.65°, which can be related to $MoO_n{\cdot}mH_2O$ and other compounds of Tb–Mo–O, as Tb_2MoO_6. However, we added the ICSD 79808 (Tb_2MoO_6) and ICSD 2859 ($MoO_3{\cdot}2H_2O$) files to compare them with the extra peaks (see Fig. S1 in supplementary material) and found that the extra peaks corresponded to ICSD 2859 and not ICSD 79808. The extra phase was formed because of the rare-earth solubility limit in the $CaMoO_4$ crystal structure. This observation is in agreement with the observation of Parchur and Ningthoujam [54]. In addition, an indication of the successful substitution of Tb^{3+} for Ca^{2+} in the A sites (AMO_4) of $CaMoO_4$ was associated with the strongest peak at around $2\theta = 28.7°$, which corresponds to the (112) crystalline plane, showing a slight displacement to lower angles with doping of Tb^{3+} when compared with pure $CaMoO_4$ matrix. Moreover, the effect of increasing the concentration of Tb^{3+} cations was verified by the broadening of the peak corresponding to the (112) plane and a decrease in its intensity in comparison with the pure $CaMoO_4$ matrix (see Fig. 1), confirming that Tb was inserted in the lattice.

It is clear from the XRD patterns for $CaMoO_4$:$x$$Tb^{3+}$ that when a few Ca^{2+} ions are replaced by Tb^{3+} ions, the lattice structure slightly changes because of the ionic radius of Tb^{3+} (1.04 Å), which is slightly smaller than the ionic radius of Ca^{2+} (1.12 Å) [55,56]. This behavior was justified by Almeida et al. [39], who stated that the cationic substitution causes vacancies to be created and that these defects present in the $CaMoO_4$ lattice are responsible for the changes recorded in the

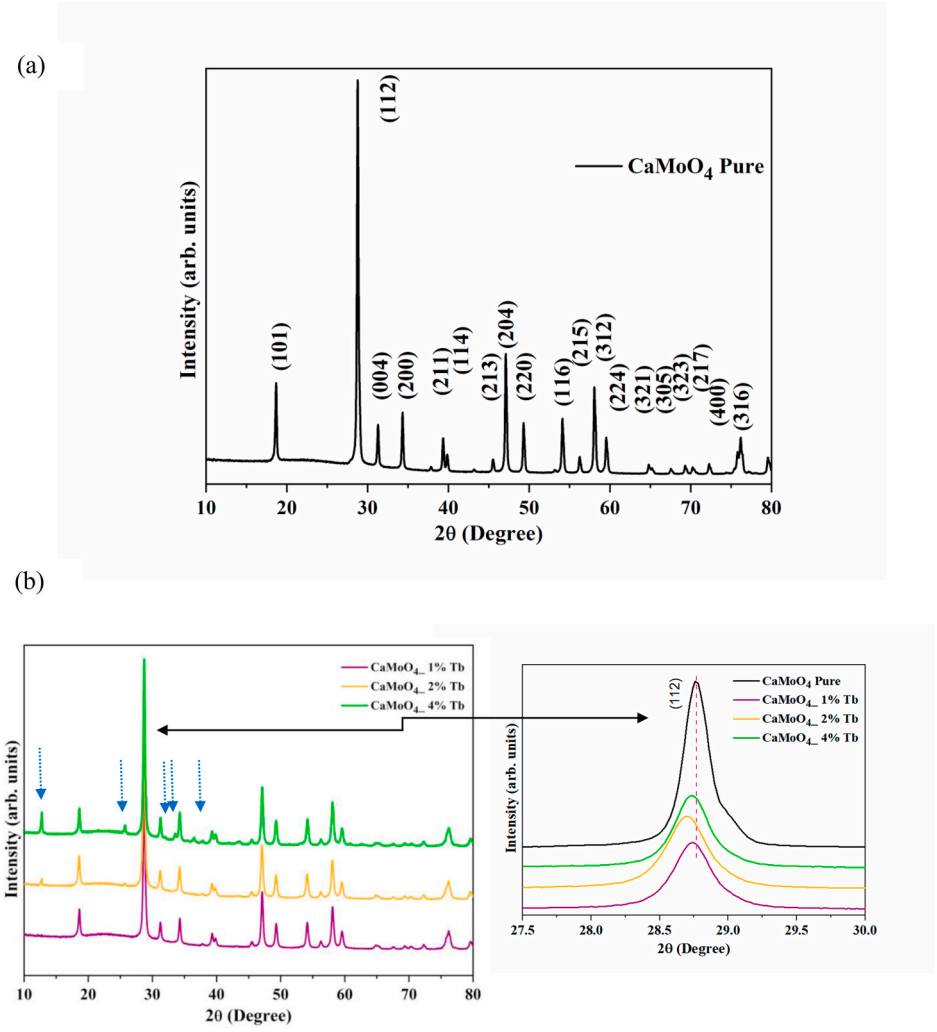

Fig. 1. X-ray diffraction patterns of (a) pure $CaMoO_4$ and (b) $CaMoO_4$:$x$$Tb^{3+}$ (x = 1 mol%, 2 mol%, and 4 mol%) powder samples prepared by spray pyrolysis at 1000 °C.

scheelite-type structure. The effect of increasing the concentration of Tb^{3+} in the $CaMoO_4$ network was verified by the increase in the number of diffraction peaks and the reduced intensity, especially for the peak corresponding to the (112) plane, as shown in Fig. 1.

In addition, the high-quality powder diffraction data, in combination with the Rietveld method, allowed the refinement of a structural model (atomic coordinates, site occupancies, and atomic displacement parameters), as well as the profile parameters (lattice constants, peak shape, sample height, and background). The occupation sites of Ca^{2+} and Tb^{3+} for 1 mol%, 2 mol%, and 4 mol% concentration in the crystal lattice as calculated by the Rietveld refinements are presented in Table S1, and the good quality of the structural refinements is evidenced by the low deviations of the statistical parameters (R_{Bragg}, R_p, and χ^2) in Table 1.

The Rietveld refinement results indicate that the diffraction patterns obtained for the $CaMoO_4$:xTb^{3+} crystals match the corresponding spectra in the ICSD 60552 file, as shown in Fig. 2. Besides, the theoretical lattice parameters and the unit cell volume calculated at the B3LYP level of theory showed good agreement with the experimental results. The lattice parameters and, consequently, the unit cell volume of the samples changed with Tb^{3+} doping variation (Table 1). This occurred because of the cationic substitution of Tb^{3+} for Ca^{2+}, which caused slight distortions of the unit cell because of the Tb^{3+} cations having a smaller ionic radius than the Ca^{2+} cations [57], electronic valence difference, and also the presence of vacancies that can act to promote local structural disorders that increase the unit cell volume.

As discussed above, the Tb^{3+} doping of pure $CaMoO_4$ is supported by the presence of calcium vacancies, which balance the excess charge and neutralize the system, following the equation for defects:

$$CaMoO_4 + Tb(III) \rightarrow Ca_{1-x}Tb_xMoO_4 + xV_{Ca}, \quad (1)$$

where V_{Ca} represents a calcium vacancy.

A schematic representation in terms of the component clusters, the cation replacement and vacancy formation mechanisms associated with the doping process, and the crystalline structure of $CaMoO_4$:xTb^{3+} is illustrated in Fig. 3. In addition, the corresponding values of the atomic coordinates (x, y, z) are listed in Table S2. Moreover, the theoretical bond distances obtained from the optimized model at the B3LYP level of theory successfully described the crystalline environment for Ca, Tb, and Mo centers, confirming the existence of [CaO_8], [TbO_8], and [MoO_4] clusters, respectively, as predicted by the experimental data.

Table 1
Lattice parameters, unit cell volume, and statistical parameters of $CaMoO_4$:xTb^{3+} (x = 1 mol%, 2 mol%, and 4 mol%) microspheres obtained by Rietveld refinement. Theoretical values obtained for the Tb-doped model (unit cell) are included for comparison.

Sample	Cell volume (Å$_3$)	Lattice parameters	
		$\alpha = \beta = \gamma = 90°$ ($I4_1/a$)	
		$a = b$ (Å)	c (Å)
$CaMoO_4$:xTb^{3+}			
x = 1 mol%[a]	312.4	5.226	11.44
x = 2 mol%[b]	312.5	5.227	11.43
x = 4 mol%[c]	312.1	5.227	11.43
ICSD 60552 $CaMoO_4$	311.5	5.222	11.42
Theoretical	309.8	5.236	11.30
R_{Bragg} (%) = 6.75[a], 11.94[b], 7.23[c]; χ^2 (%) = 1.701[a], 1.723[b], 1.670[c]; R_p (%) = 12.49[a], 14.86[b], 10.49[c].			
D (nm) = 21.4[a], 22.1[b], 22.5[c]; $\mathcal{E}$ (10^{-3}) = 0.80[a], 0.78[b], 0.78[c].			

This study is of particular significance because it provides deep insight into the photoinduced mechanism responsible for the luminescence properties of Tb^{3+}-doped $CaMoO_4$ samples obtained by the ultrasonic spray pyrolysis method. The combination of experimental techniques with high-throughput density functional theory calculations enables us to correlate the superior optical properties with the existence of a singular chemical environment on the basis of the structural composition, electronic structure, and excited states.

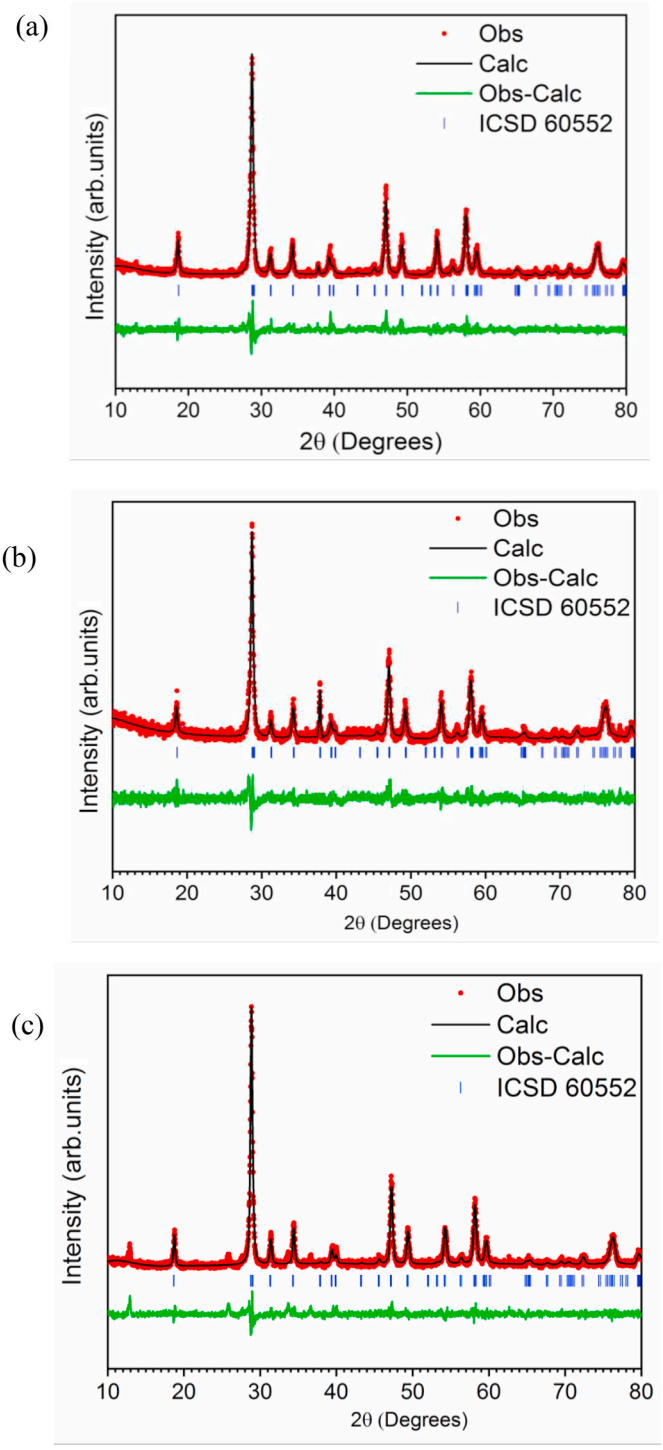

Fig. 2. Structural refinement of the $CaMoO_4$:xTb^{3+} samples: (a) x = 1 mol%; (b) x = 2 mol%; (c) x = 4 mol%.

FEG-SEM images of the $CaMoO_4$ and $CaMoO_4$:xTb^{3+} (x = 1 mol%, 2 mol%, and 4 mol%) microspheres are shown in Fig. 4. Fig. 4 shows microspheres formed by nanoparticles, where this morphology results from several physicochemical phenomena that occur simultaneously in the USP method. The solubility in water and the melting point of calcium nitrate and terbium nitrate are 1.44 g mL^{-1} and 561 °C and 1.57 g mL^{-1} and 89 °C, respectively [37]. In addition, the high water solubility of the metal nitrates makes the precursor solution highly supersaturated, generating a large number of nanocrystals that bind to form the microspheres [58]. The stoichiometric increase of terbium nitrate in the

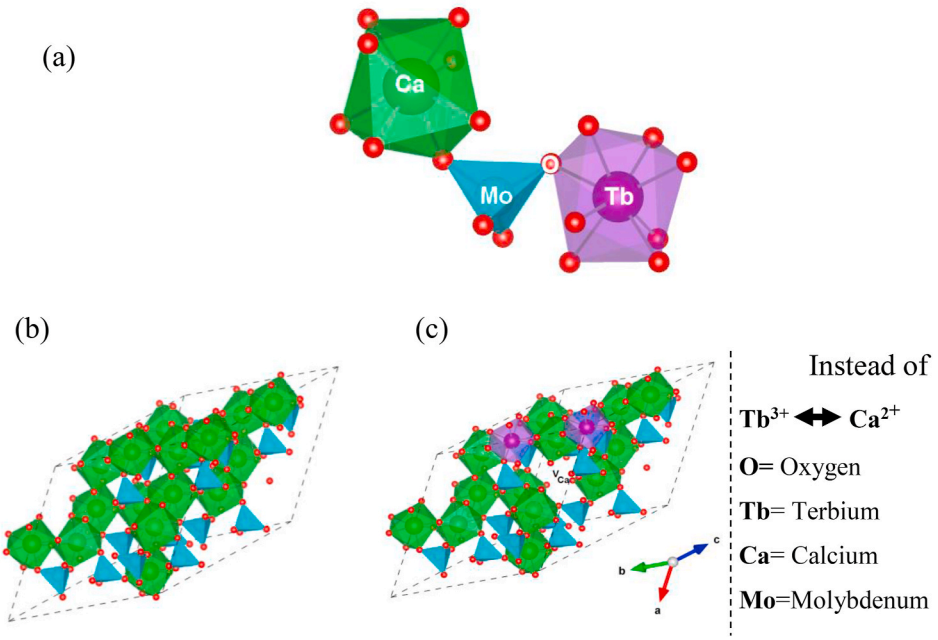

Fig. 3. (a) Representative structure of $[MoO_4]$, $[TbO_8]$, and $[CaO_8]$ polyhedral clusters, (b) 2 × 2 × 2 supercell of pure $CaMoO_4$, and (c) 2 × 2 × 2 supercell of $CaMoO_4$ with Tb^{3+} cation inserted. V_{Ca}, calcium vacancy.

precursor solution promoted trapping of water by the calcium/terbium compound molten salt because of the low melting point of terbium nitrate in water, and the high temperature caused an increase in water vapor pressure inside the particle, which promoted generation of porous spherical particles, irregular porous particles, and rough particles by escape of water vapor. Thus, the increase in the amount of Tb in the precursor solution modifies the solubility of the solution and the behavior of the physicochemical phenomena, thereby resulting in deformed microspheres and more dispersed nanocrystals (Fig. 4c and d).

These microspheres have high defect density because of the interfaces between the nanoparticles forming the microspheres. Thus, the USP method, at the same time as being a way to produce nanoparticles, organizes the interfaces of the nanoparticles to form the microspheres, and consequently modifies their physical and chemical properties.

The structural behavior of pure $CaMoO_4$ and $CaMoO_4$:xTb^{3+} powders was analyzed by means of the Raman spectra. The Raman spectra in Fig. 5a show sharp peaks for external and internal modes for $CaMoO_4$ treated at 1000 °C (treatment at 600 °C was reported by Almeida et al. [39]), indicating that the synthesized powders were highly crystallized with short-range order.

There are 26 vibrational modes characteristic of the scheelite phase in the tetrahedral structure: Γ (Raman + infrared) = $3A_g + 5_{Au} + 5_{Bg} + 3_{Bu} + 5_{Eg} + 5_{Eu}$, with A_g, B_g, and E_g being the Raman-active modes [21,25,59]. As illustrated in Fig. 5a, the Raman spectra of $CaMoO_4$ reveal ten Raman-active phonon modes with short-range order, whereas the other vibrational modes (B_g and A_g) are not detected, probably because of their low intensities.

Fig. 5a shows the Raman spectra of the $CaMoO_4$ and $CaMoO_4$:xTb^{3+} microspheres in the range from 100 cm^{-1} to 1000 cm^{-1}. The modes can be classified either as internal vibrations (the center of mass of $[MoO_4]^{2-}$ does not move) or as external vibrations (motion of the Ca^{2+} cations and the movements of the $[MoO_4]^{2-}$ tetrahedra as rigid units). These microspheres presented several peaks corresponding to the Raman-active internal modes of MoO_4 tetrahedra, being ν_1 (A_g), ν_3 (B_g), ν_3 (E_g), ν_4 (E_g), ν_4 (B_g), ν_2 (B_g), ν_2 (A_g), R (A_g), R (E_g), and external T (B_g E_g E_g), which are in agreement with the published literature [39].

One high-frequency band centered at 882 cm^{-1} for $CaMoO_4$:xTb^{3+} was observed, corresponding to intense peaks in the Raman (A_g) mode, and is assigned to the symmetric stretching ν_1 (A_1) of the bonds, while the two Raman (B_g and E_g internal) modes at 850 cm^{-1} and 797 cm^{-1} are attributed to the asymmetric stretching of the bonds.

The experimental Raman-active modes shown in Fig. 5a indicate the existence of a strong interaction between the ions arising from the stretching and bending vibrations of the shorter metal–oxygen bonds within the anionic groups. Doping with Tb^{3+} cations promotes a slight decrease in the intensity in the Raman spectra, and we also observed vibrational modes that were not detected in the Raman spectra for $CaMoO_4$:xTb^{3+} compared with pure $CaMoO_4$ (192 cm^{-1} and 406 cm^{-1}): see Fig. 5b. This is explained by an increase in local disorder of the shorter metal–oxygen bonds.

4.2. Optical properties

Optical properties such as PL are strongly dependent on the structural and morphological features of the crystal system [4,13,14]. In addition, we believe that the E_{gap} values can also be related to factors such as morphology, as well as particle shape and size and even doping. Besides the morphological aspects, the optical phenomena of any semiconductor can be modified by introducing impurities or dopants into its crystalline lattice [60].

The optical properties of the $CaMoO_4$:xTb^{3+} (x = 1 mol%, 2 mol%, and 4 mol%) microspheres prepared by the USP method were investigated by their UV–vis absorption and photoluminescent emissions at room temperature. With the partial replacement of Ca^{2+} by Tb^{3+} ions, a considerable change in the crystalline environment can occur involving the electronic and structural properties of materials, as shown in Fig. 6.

The energies presented in Fig. 6 were determined by the Wood and Tauc method [61]. The results of the experiments show that E_{gap} decreased from 3.87 eV (pure) to 3.72 eV and 3.55 eV on going from $CaMoO_4$ to $CaMoO_4$ doped with 1 mol% and 2 mol% Tb^{3+}, while it increased to 3.90 eV for 4 mol% Tb^{3+}. This result is associated with a marked E_{gap} reduction (3.87 eV), which is attributed to the high density of defects introduced by the substitution of Tb^{3+} cations for Ca^{2+} cations. The increased bandgap of $CaMoO_4$ doped with 4 mol% Tb^{3+} can be explained by the Burstein-Moss effect [62], where an increase in the Fermi level in the conduction band leads to bandgap widening with increasing carrier concentration (i.e., doping with 4 mol% Tb^{3+} may have generated a large number of defects, but the greatest occupation

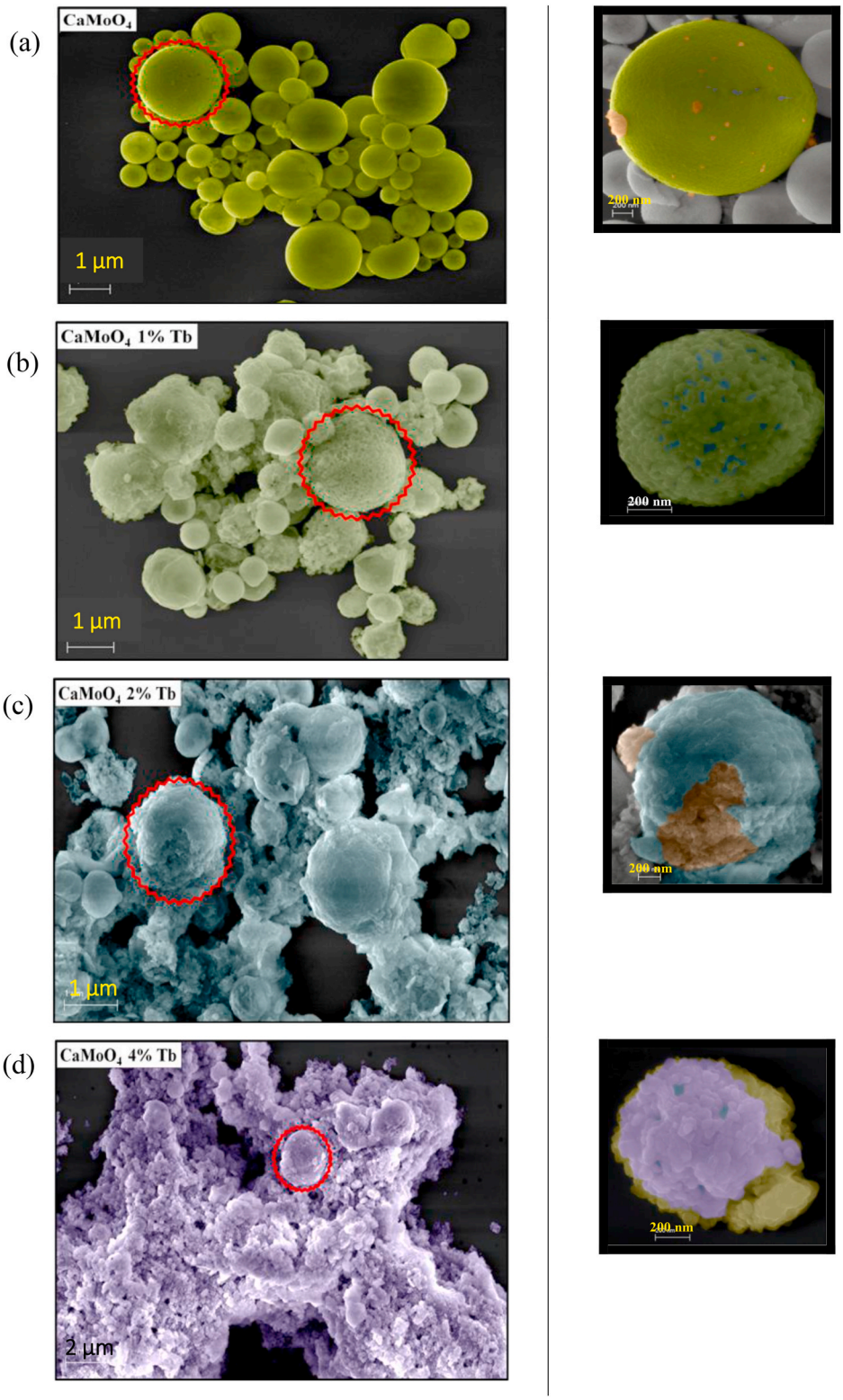

Fig. 4. Field-emission gun scanning electron microscopy images of (a) $CaMoO_4$ microspheres and $CaMoO_4$:xTb^{3+} microspheres with (b) $x = 1$ mol%, (c) $x = 2$ mol%, and (d) $x = 4$ mol%.

occurred at the edge of the conduction band, which resulted in an apparent increase in the bandgap).

In this context, we propose a general mechanism associated with the optical properties of $CaMoO_4$:Tb^{3+} crystals. First, in the electronic excitation mechanism, a structural disorder connects the singlet ground state to the singlet excited state (s*) by a perturbation of the valence band maximum (VBM) and conduction band minimum (CBM). In particular, this electronic disorder follows the cation displacement (0.1 Å, Ca atom) along the Ca–O–Tb–O–Mo intermetallic connection, in accordance with the volume change from 2478.66 $Å^3$ to 2478.92 $Å^3$ accompanying order-disorder effects in the constituent clusters (see Table S3). Furthermore, the complete structural reorganization

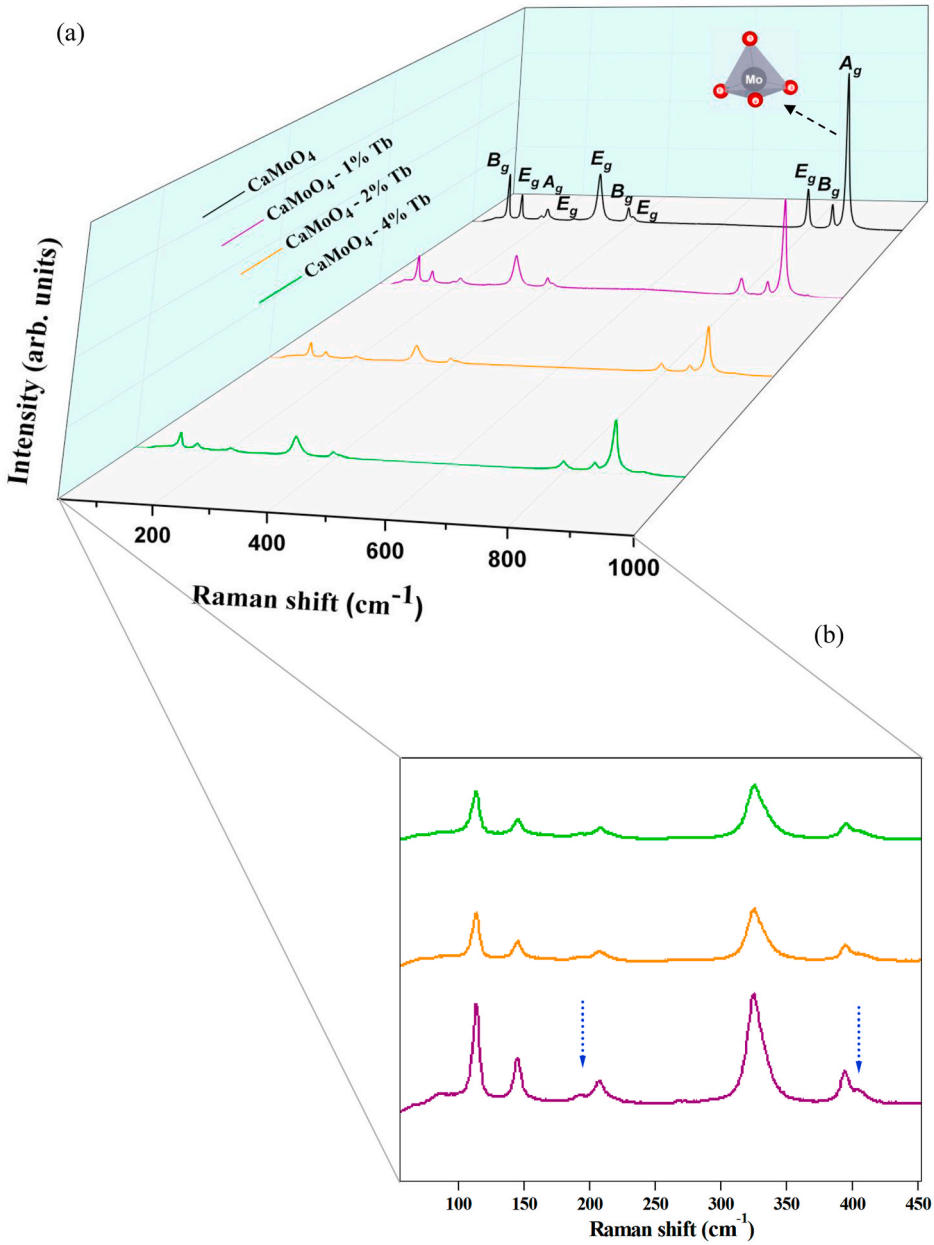

Fig. 5. (a) Raman spectra of pure $CaMoO_4$ and $CaMoO_4$:$x$$Tb^{3+}$ ($x = 1$ mol%, 2 mol%, and 4 mol%) microspheres obtained by spray pyrolysis at 1000 °C and (b) peak magnification in the region from 100 cm^{-1} to 450 cm^{-1}.

associated with the spin splitting in the triplet excited state (t*) induces an exciton separation on the valence band and conduction band, being such excitons trapped mainly in the empty orbitals of Tb and Mo cations, respectively. In particular, this process describes the relaxation of order-disorder effects (see Table S3), followed by a volume contraction to 2473.54 $Å^3$.

In previous studies [63], we showed that the defect-induced bandgap (E_{gap}) reduction in crystalline structures is associated with intermediate electronic levels introduced in the bandgap. Such a mechanism has been improved greatly with the description of s^* and t^* states. We consider such electronic states as the quantum evidence of electron-hole pair generation in solid-state theory (see Fig. 7).

Initially, the Tb^{3+} doping in $CaMoO_4$ induces the formation of calcium vacancies that perturb the VBM energy levels, and promotes the insertion of 4f orbitals in the CBM. Intermediate energy levels are introduced in the E_{gap} region, reducing the energy required for electron transfer. The next step is the photoinduced electron transfer from the VBM to the CBM, generating an electron-hole pair within the $CaMoO_4$:Tb^{3+} electronic structure (Fig. 7). This step is crucial because it offers a new interpretation of the optical properties of a material.

Then, to clarify the electronic structure of $CaMoO_4$:$x$$Tb^{3+}$, for each case, the optimized structure was analyzed; the most important geometrical parameter values are reported in Tables S2 and S3. Furthermore, the total and atomic orbital–resolved DOS profiles and the band structure profiles were obtained; the corresponding results are presented in Fig. 8. The band structure and the total and 4f atomic orbital (Tb) DOS profiles for $CaMoO_4$:$x$$Tb^{3+}$ are presented for the singlet ground state (s), the singlet excited state (s*), and the triplet excited state (t*) in Fig. 8a–c, respectively.

For the singlet ground state (s), the singlet excited state (s*) and the triplet excited state (t*), Fig. 8 shows that the upper region of valence bands correspond mainly to 2p (O) orbitals and have a weak contribution from cationic states; the lower region of conduction bands consist mainly of 4d (Mo) and 4f (Tb) orbitals with a slight contribution from 2p

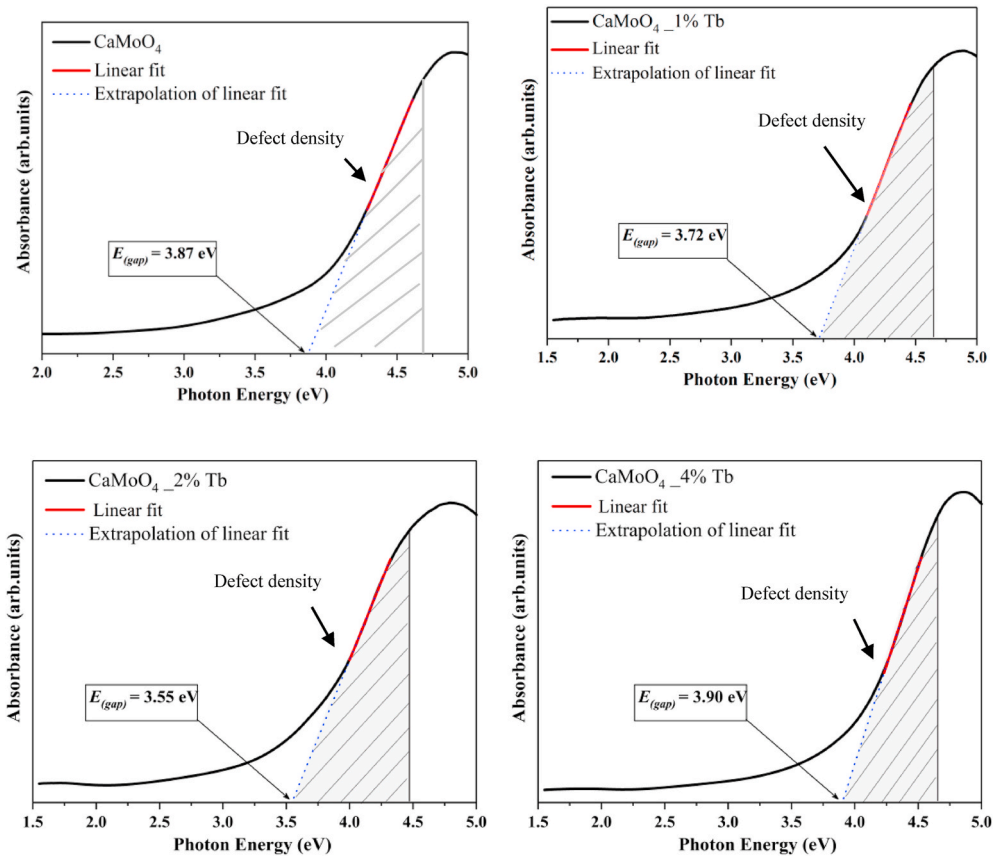

Fig. 6. Determination of the gap by the Wood and Tauc method for $CaMoO_4$ and $CaMoO_4$:xTb^{3+} (x = 1 mol%, 2 mol%, and 4 mol%) microspheres synthesized by spray pyrolysis at 1000 °C.

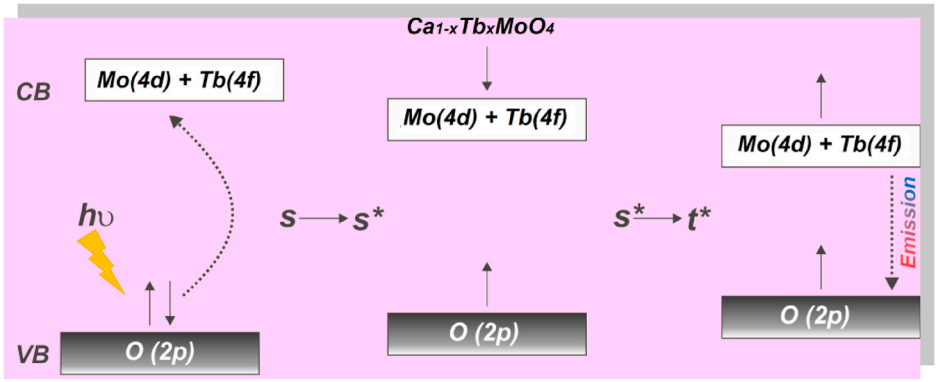

Fig. 7. Energy levels of the ground and excited states of $Ca_{1-x}Tb_xMoO_4$. CB, conduction band; s, singlet ground state; s*, singlet excited state; t*, triplet excited state; VB, valence band.

(O) orbitals. The $4f^2_{xz}$, $4f^2_{yz}$, $4f^2_{y(3x^2-y^2)}$, and $4f_{xyz}$ (Tb) orbitals mainly dominate the bottom of the conduction band, and there is a small content of $4f^2_{x(x^2-3y^2)}$ orbitals for $CaMoO_4$:xTb^{3+} (s), whereas $4f^2_{yz}$, $4f^3_z$, $4f^2_{y(3x^2-y^2)}$, $4f_{xyz}$, and $4f^2_{x(x^2-3y^2)}$ also contribute to the bottom conduction band of the s* structure. Notice that the emergence of $4f^3_z$ participation in the s* model can be attributed mainly to a displacement of 0.1 Å in the z direction. Furthermore, the DOS shape is significantly changed in the conduction band region, which indicates that the excited singlet configuration applied over the distorted structure generates the recombination of eigenfunctions in the overall structure.

The band structure analysis for the triplet state and its corresponding DOS illustrated in Fig. 8c shows that the direct observations of triplet band structure result in the conclusion that α electrons are mainly responsible for the top of valence band formation and that β electrons are mainly responsible for the bottom of conduction band, corresponding to O 2p, Mo 4d, and Tb 4f contributions, respectively. These assumptions can be seen on the right in Fig. 8c for the $CaMoO_4$:xTb^{3+} triplet DOS.

In addition, the band structure profiles obtained indicate that the VBM and CBM regions both have flat energy bands against the symmetry points, resulting in a small difference between the direct and indirect bandgaps, which helps achieve superior electrical and optical properties. According to theoretical calculations, the relative energies of the s* and t* excited states (from spin α to spin β) to the s ground state are 3.96 eV (Γ-N indirect bandgap), 2.14 eV (Γ-Γ direct bandgap), and 3.97 eV (Γ-Z indirect bandgap) (see Fig. 8).

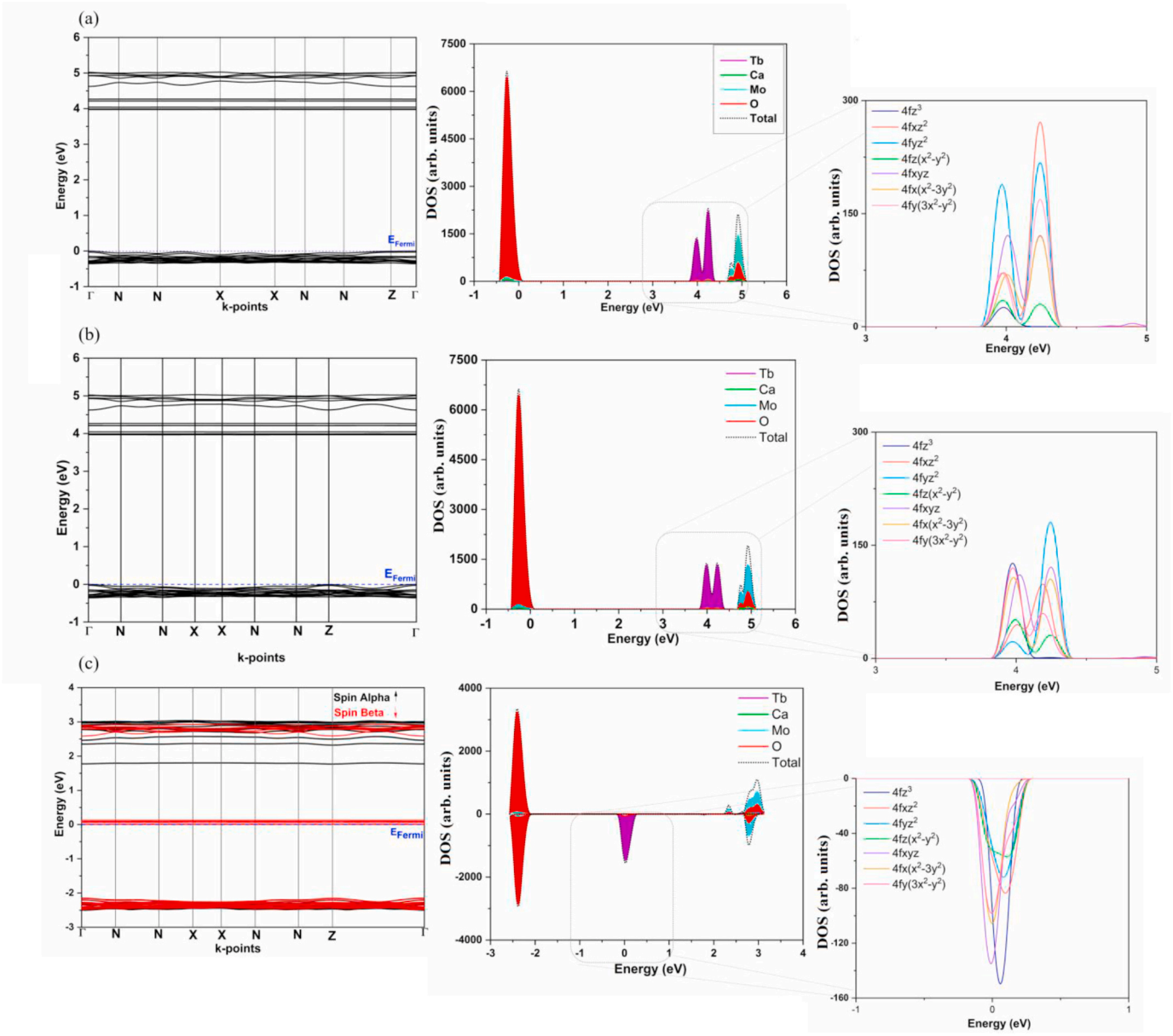

Fig. 8. Band structure and total and atomic orbital–resolved density of states (DOS) profiles for (a) the singlet ground state (s), (b) the singlet excited state, and (c) the triplet excited state of $CaMoO_4$:$x$$Tb^{3+}$.

A considerable decrease of the bandgap is observed (0.1 eV in s* and 1.83 eV in t*) with respect to the s ground state. In the fundamental [MoO_4], [CaO_8], and [TbO_8] clusters the distortion of the excited tetrahedral and deltahedral groups favors the formation of intermediate energy levels in the conduction band, which results in the bandgap of this material. In addition, the cation polyhedra in the s ground state and the s* and t* excited states have slight different metal–oxygen distances; that is, O_{92}–Tb_2 distance of 2.374 Å, O_{92}–Mo_5 distance of 1.827 Å, and O_{92}–Ca_{13} distance of 2.429 Å for the s ground state, O_{92}–Tb_2 distance of 2.374 Å, O_{92}–Mo_5 distance of 1.828 Å, and O_{92}–Ca_{13} distance of 2.432 Å for the s* state, and O_{92}–Tb_2 distance of 2.305 Å, O_{92}–Mo_5 distance of 1.840 Å, and O_{92}–Ca_{13} distance of 2.429 Å for the t* state as demonstrated in Fig. S2 and Table S3. This difference, as mentioned in the discussion of the XRD data, is associated with the ionic radii being different, and the vacancy generated in the material promotes a structural defect that is responsible for facilitating electronic transitions within the bandgap. Despite the introduction of 4f levels in the bandgap region, the additional structural distortions can affect both the VBM and the CBM through a new distribution of the electronic density associated with the balance of attractive and repulsive forces that act on the chemical bonds [63,64].

In recent decades, Dorenbos, Boutinaud, Cavalli, and coworkers [65–70] conducted an extensive study on the luminescence properties of trivalent lanthanide ions (Ln^{3+}) using a spectroscopic method to obtain information on the Ln^{3+} ground-state energy location. They particularly studied the so-called intervalence charge transfer (IVCT); that is, the transfer of an electron from the ground 4f state of trivalent lanthanide ions (Ce^{3+}, Pr^{3+}, Eu^{3+}, Tb^{3+}, Tm^{3+}, Yb^{3+}, etc.) to a transition metal ion. Detailed knowledge of these processes is important to assess the possible applications of these compounds and for a better understanding of their excited-state dynamics.

According to the empirical equation proposed by Cavalli et al. [5], with use of the energy of the IVCT band observed in excitation spectra of Tb^{3+} emission in transition metal compounds, information is obtained on the location of the ground-state energy of Tb^{3+} with respect to the valence and conduction bands. Specifically, in molybdates and

tungstates, the ground state of Tb^{3+} is located in the forbidden bandgap close to the conduction band.

Besides, the relations of the optical transition probabilities in rare-earth Ln^{3+} ions incorporated in the host lattice can be understood by use of crystal field analysis. Following this approach, the energy of the $4f^{n-1}5\ d^1$ electronic configuration of the Ln^{3+} ion in the lattice is expected to be shifted with respect to that of the free ion because of the interaction of the d electron with a host. Further, since d electrons are much more extended than f electrons, the energy of the lowest state of the $4f^{n-1}5d$ electronic configuration of the Ln^{3+} ion in the lattice is expected to be diminished with respect to that of the free ion by the quantity of centroid shift and crystal field splitting [71]. Moreover, the relative energy of the ground state of the given Ln^{3+} with respect to the valence band and conduction band edges depends on the host lattice, and the ion–ligand distance *R*. Furthermore, in other previous work, the optical properties of rare-earth ions (Tm^{3+} [72], Sm^{3+} [73], and Eu^{3+} [74]) were studied, and the crystal field and free ion parameters were calculated.

From a theoretical point of view, the description of the crystal field and IVCT mechanism [5,75] can be associated with the localization of ground and excited electronic states inside the bandgap region of the host matrix. At first glance, the ground state for $CaMoO_4$:$x$$Tb^{3+}$ was calculated to be located in the vicinity of the CBM (Fig. 8a), as predicted by experimental analysis. Additionally, the IVCT mechanism can be visualized in the DOS profiles for the s* and t* states, where a clear electron transfer mechanism is due to the presence of unpaired electrons in Tb and Mo valence states, confirming the intermetallic transfer described as the redox process $Tb^{3+} + Mo^{6+} \rightarrow Tb^{4+} + Mo^{5+}$. As a consequence, the energy levels of Tb and Mo are displaced in energy (Fig. 8c); in particular, the Mo 5d state becomes a nondegenerate state in the vicinity of the CBM, while Tb 4f states are shifted close to the Fermi level. Moreover, Fig. S2 helps us to localize such charge transfer in the Ca–O–Mo–O–Tb bond path due to the strong localization of the unpaired electron isosurface on the Tb and Mo cations neighboring the calcium vacancy. Therefore, the combination of first-principles calculations for ground and excited electronic states, crystal field analysis, and IVCT analysis can provide deep insight into the optical properties of the $CaMoO_4$:Tb^{3+} matrix.

Furthermore, the PL spectra can be used to investigate how the optical properties are affected by the Tb^{3+} doping process because defects in the crystal lattice play an important role in the determination of the luminescence properties of oxides [76]. Therefore, the direct changing

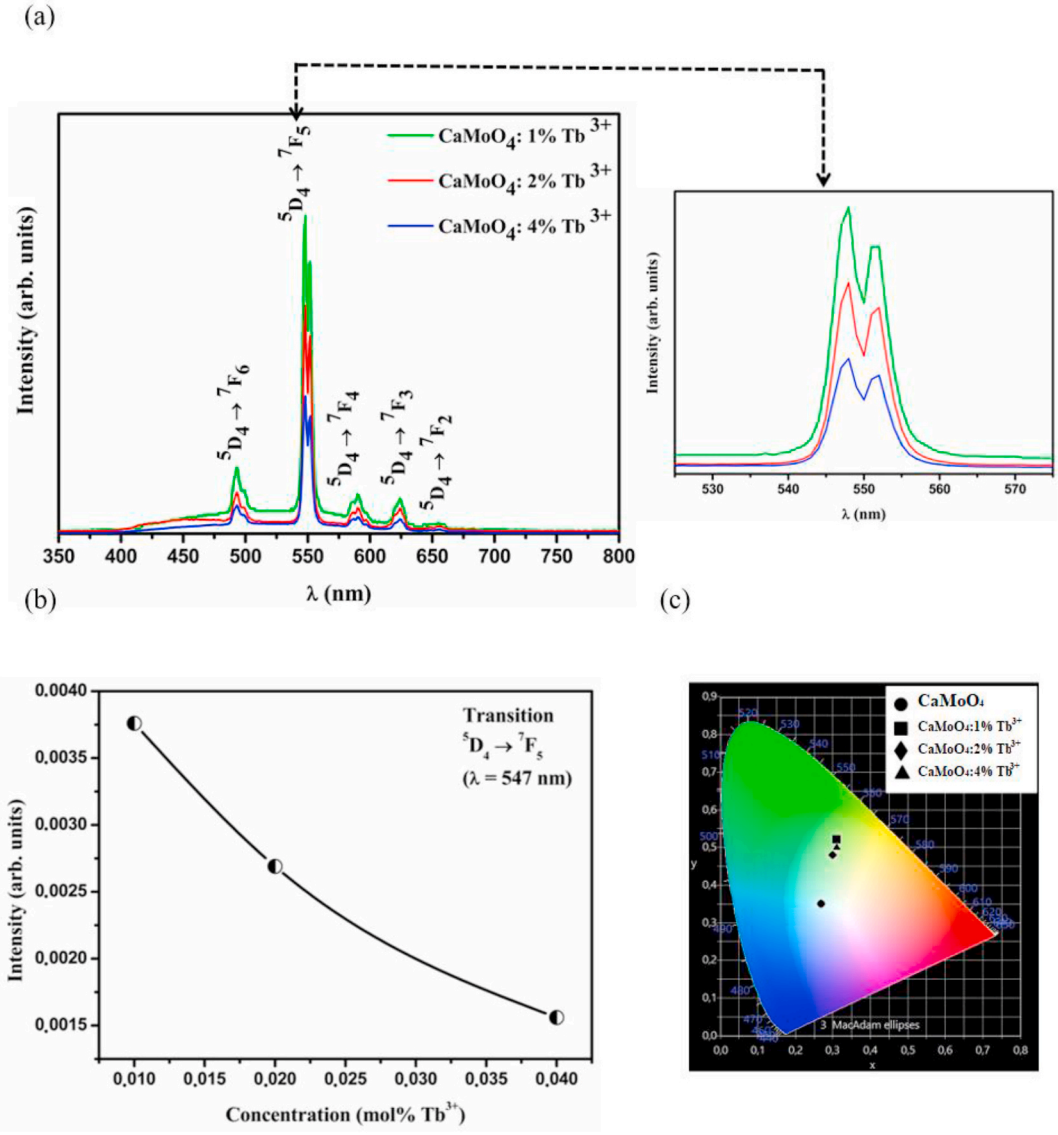

Fig. 9. (a) Photoluminescence spectra of $CaMoO_4$:$x$$Tb^{3+}$ (x = 1 mol%, 2 mol%, and 4 mol%) microspheres. (b) Relationship between photoluminescence intensity and concentration of Tb^{3+}. (c) CIE chromaticity diagram for pure CaMoO and $CaMoO_4$:$x$$Tb^{3+}$.

of the contents of some types of defects may cause variations in the concentrations of the corresponding luminescence centers, according to Shi et al. [77] and Selvalakshmi et al. [78]. In particular, the calcium and/or oxygen vacancies formed, which serve as electron- or hole-trapped centers, might act as sensitizers for the energy transfer from the host to the Tb^{3+} ions and enhance the luminescence intensity. The PL spectra of $CaMoO_4$:xTb^{3+} (x = 1 mol%, 2 mol%, and 4 mol%) crystals are shown in Fig. 9.

We suggest that there is a relationship between the PL intensity and the amount of Tb^{3+} ions in the $CaMoO_4$ matrix, which is due to the coordination environment and/or changes in the shape of the crystals since an increase of the Tb^{3+} concentration also leads to changes in the host morphology (Fig. 4). In addition, it is well known that photoluminescence is associated with the structural and electronic distortion of the MoO_4 tetrahedron, with concomitant appearance of intermediate levels of the bandgap, as well as Raman-active phonon modes of short-range order. Therefore, with the Tb^{3+} doping process associated with the generation of vacancies, a significant number of structural defects in the crystalline lattice are expected, which is considered a critical factor for the PL properties [79]. Under this condition, electronic transitions occur more easily, thus favoring photoluminescence.

In addition, pure $CaMoO_4$ samples exhibit a broadband PL behavior with white light emission according to the calculated values of the CIE coordinates at 1000 °C (x 0.37, y 0.37), as reported by Almeida et al. [39]. The PL spectra of $CaMoO_4$:xTb^{3+} depicted in Fig. 9a reveal five characteristic emission bands of Tb^{3+} ions [80], which are observed at 493 nm ($^5D_4 \rightarrow {}^7F_6$), 545.5 nm ($^5D_4 \rightarrow {}^7F_5$), 590 nm ($^5D_4 \rightarrow {}^7F_4$), 624 nm ($^5D_4 \rightarrow {}^7F_3$), and 655 nm ($^5D_4 \rightarrow {}^7F_2$).

In this perspective, Cavalli et al. [5] reported the optical spectra of $CaMoO_4$ crystals doped with Tb^{3+} by the flux growth method. Their luminescence properties were investigated in the temperature range from 10 K to 600 K under different experimental conditions, and the processes governing the luminescence dynamics were analyzed, confirming that this aspect is important and deserves a thorough investigation.

The luminescence spectra presented in this work are in accordance with the spectra reported by Cavalli et al. [5]; however, they also observed the spectrum produced by excitation at a different wavelength is very similar. In addition, the decay profiles of $^5D_4$ emissions were measured as a function of the temperature, with decay times ranging from 460 μs to 520 μs.

Recently, $CaMoO_4$:xTb^{3+} nanoparticles (x = 1 atom %, 3 atom %, 5 atom %, 7 atom %, 10 atom%, 15 atom%, and 20 atom%) were reported by Parchur et al. [81]. The luminescence intensity of the 4f → 5d transition reported by Parchur et al. is in accordance with our observation. We find the emission intensity of the $^5D_4 \rightarrow {}^7F_5$ transition at approximately 546 nm is in excellent agreement with the value reported by Parchur et al. (547 nm) as the highest among the other transitions. Furthermore, a change in emission intensity of the $^5D_4 \rightarrow {}^7F_5$ transition (547 nm) with Tb^{3+} concentration (1 atom %, 3 atom %, 5 atom %, 7 atom %, 10 atom %, 15 atom %, and 20 atom % Tb^{3+}) at 355 nm was also observed. In addition, the luminescence decay of the $^5D_4$ level under 355 nm excitation shows biexponential behavior, indicating the availability of Tb^{3+} ions on the surface and in core regions of the particle.

The excitation and emission spectra of $CaMoO_4$:xTb^{3+} (x = 1 mol%, 3 mol%, 5 mol%, 7 mol%, 9 mol%, 15 mol%, and 20 mol%) were reported by Zhou et al. [76]. In this case, the PL spectra produced by excitation at 299 nm (Tb^{3+}, $^5D_4 \rightarrow {}^7F_5$) showed the charge transfer band of Mo–O in the excitation spectrum of Tb^{3+}-doped phosphor. Moreover, monitoring the emission of Tb^{3+}, the authors illustrates the presence of energy transfer from the host to activator Tb^{3+}. The emission spectra of the green phosphors with various doping concentrations for an excitation wavelength of 299 nm were similar to our spectra, with four characteristic transitions of Tb^{3+} clearly located at 488 nm, 544 nm, 587 nm, and 622 nm belonging to the $^5D_4 \rightarrow {}^7F_J$ (J = 6, 5, 4, and 3) transition.

After $CaMoO_4$:Tb^{3+} is excited at 350 nm, the [MoO_4] clusters absorb part of this excitation energy by presenting a favorable energy configuration allowing better absorption. Later, this energy is transferred to the Tb^{3+} ions. This behavior was determined by Park et al. [82], who considered the contribution of the $SrMoO_4$ matrix in the PL behavior of the Tb^{3+}-doped material. According to the results shown in Fig. 9a, the well-defined transitions of Tb^{3+} show that the energy transfer between [MoO_4] and Tb^{3+} was successful.

This transition has a characteristic emission line corresponding to the $4f^n \rightarrow 4f^n$ transition of the terbium ion, which is induced by the change in the chemical environment of Tb^{3+} ions during the formation of a chemical bond between the host and the Tb^{3+} ion. This is associated with the charge transfer from tetragonal $[MoO_4]^{-2}$ clusters to the [TbO_8] clusters contributing to 4f → 5d transitions of Tb^{3+} [8,25,83,84]. As a result, the peaks found from approximately 490 nm to approximately 660 nm are associated with Tb^{3+} $^5D_4 \rightarrow {}^7F_J$ (J = 6, 5, 4, 3, and 2) transitions, which may result in green emission [26,85].

The performance of rare-earth ion–doped photoluminescent materials can be considerably affected by the concentration of dopants [86]. It is observed in Fig. 9a that as the concentration of Tb^{3+} increases, the PL intensity decreases. This behavior, known in the literature as the *quenching concentration*, is promoted by the approximation of Tb^{3+} ions favoring nonradioactive processes in energy transfer dynamics, causing PL suppression. Fig. 9b shows the relationship between PL intensity and Tb^{3+} concentration.

Therefore, $CaMoO_4$ and $CaMoO_4$:xTb^{3+} microspheres with intrinsic defects (cation vacancies) and interfaces modulate the bandgap of the material and improve the optical (PL) and chemical (organic photodegradation) properties.

Förster resonance energy transfer (FRET) occurs when the activator (or sensitizer) is in the excited state. FRET is based on the classic dipole-dipole interactions between transition dipoles of the donor and acceptor and is significantly dependent on the donor-acceptor distance, falling at a rate of $1/R^6$. FRET can typically occur at distances up to 100 Å [87]. Dexter energy transfer is a short-range phenomenon (critical distance 10 Å) that decreases with e^{-R} and depends on the spatial overlap of sensitizing and inhibiting molecular orbitals. Blasse [88] assumed that for the quenching concentration, the shortest average distance between the closest activating ions is equal to the critical distance. The critical distance can be calculated with Eq. (2):

$$CD = 2x\left(\frac{3V}{4\pi X_c N}\right)^{1/3} \quad (2)$$

where X_c is the quenching concentration, N is the number of units of the molecular formula per unit cell, and V is the unit cell volume. V and N for the crystalline $CaMoO_4$ (tetragonal system, one cell unit of $CaMoO_4$ comprising four formula units) are 312.40 $Å^3$ and 4, respectively (ICSD 60552). For X_c = 0.1% (0.001), the critical distance in $CaMoO_4$:Tb^{3+} particles was calculated to be 38.94 Å. In this case, the rare-earth ion distance is greater than 10 Å. Thus, exchange interactions are ruled out. Therefore, electric multipolar interaction is believed to be the only mode for energy transfer among the rare-earth ions in $CaMoO_4$ particles.

The chromaticity coordinates are indicated in the CIE graphic, as shown in Fig. 9c. It is observed that the $CaMoO_4$ sample showed emission in the white region, whereas the $CaMoO_4$:xTb^{3+} samples evidenced a tendency for emission in the green region because Tb has its main emission ($^5D_4 \rightarrow {}^7F_5$) at around 546 nm x' and y' for the samples were as follows: 0.27 and 0.35 for $CaMoO_4$, 0.31 and 0.52 for $CaMoO_4$ doped with 1 mol% Tb, 0.30 and 0.48 for $CaMoO_4$ doped with 2 mol% Tb, and 0.31 and 0.50 for $CaMoO_4$ fopped with 4 mol% Tb.

For the calculation of the CIE chromaticity coordinates of the $CaMoO_4$:Tb^{3+} samples, the spectral power at each wavelength [$P(\lambda)$] multiplied by the weighting factor of each of the three-color matching functions is considered, [$x(\lambda)$, $y(\lambda)$, $z(\lambda)$]. The sum of these contributions gives three values called *tristimulus values* [X, Y, Z] as presented in Eqs.

(3)–(5) [89–91]:

$$X = \int_{350\ \mathrm{nm}}^{850\ \mathrm{nm}} x(\lambda)P(\lambda)d\lambda \quad (3)$$

$$Y = \int_{350\ \mathrm{nm}}^{850\ \mathrm{nm}} y(\lambda)P(\lambda)d\lambda \quad (4)$$

$$Z = \int_{350\ \mathrm{nm}}^{850\ \mathrm{nm}} z(\lambda)P(\lambda)d\lambda \quad (5)$$

The chromaticity coordinates (x', y', z') are determined from the relationships between the tristimulus values as presented in Eqs. (6)–(8). Two chromaticity coordinates are enough to characterize the emitted color.

$$x' = \frac{X}{X+Y+Z} \quad (6)$$

$$y' = \frac{Y}{X+Y+Z} \quad (7)$$

$$z' = \frac{Z}{X+Y+Z} \quad (8)$$

5. Conclusion

$CaMoO_4$:$x$$Tb^{3+}$ ($x = 1$ mol%, 2 mol%, and 4 mol%) was successfully synthesized by the USP method. The XRD analysis revealed good crystallinity and single-phase characteristics of the sample with a scheelite tetragonal phase. The introduction of Tb^{3+} cations and the creation of calcium vacancies in the $CaMoO_4$ structure resulted in a slight reduction of the bandgap. In addition, the photoluminescent emissions of the $CaMoO_4$:$x$$Tb^{3+}$ ($x = 1$ mol%, 2 mol%, and 4 mol%) samples revealed the Tb^{3+} $^5D_4 \rightarrow {}^7F_J$ ($J = 6$, 5, 4, 3, and 2) transitions, which result in green emission. FEG-SEM images revealed that the $CaMoO_4$:Tb^{3+} materials were in the form of microspheres formed by nanoparticles. According to the CIE diagram, $CaMoO_4$:$x$$Tb^{3+}$ samples evidenced a tendency for emission in the green region because Tb has its main emission ($^5D_4 \rightarrow {}^7F_5$) at around 545 nm. The charge transfer process between [TbO_8], [MoO_4], and [CaO_8] clusters is responsible for the presence of the singlet and triplet excited electronic states. In addition, the strong influence of defects (intrinsic structural defects and calcium vacancy) on electron diffusion in the samples was observed. These results summarize the relevant contributions to the understanding of the structural, electronic, and optical properties of $CaMoO_4$:$x$$Tb^{3+}$ microspheres.

Authorship contributions

Category 1

Conception and design of study: Ricardo L. Tranquilin, Marisa C. Oliveira, Anderson A. G. Santiago, Laura X. Lovisa, Renan A.P. Ribeiro, acquisition of data: Ricardo L. Tranquilin, Marisa C. Oliveira, Anderson A. G. Santiago, Laura X. Lovisa, Renan A.P. Ribeiro, analysis and/or interpretation of data: Ricardo L. Tranquilin, Marisa C. Oliveira, Anderson A. G. Santiago, Laura X. Lovisa, Renan A.P. Ribeiro, Elson Longo, Sergio R. de Lazaro, Cláudio R.R. Almeida, Carlos A. Paskocimas, Fabiana V. Motta, Mauricio R.D. Bomio.

Category 2

Drafting the manuscript: Ricardo L. Tranquilin, Marisa C. Oliveira, Anderson A. G. Santiago, Laura X. Lovisa, Renan A.P. Ribeiro, revising the manuscript critically for important intellectual content: Ricardo L. Tranquilin, Marisa C. Oliveira, Anderson A. G. Santiago, Laura X. Lovisa, Renan A.P. Ribeiro, Elson Longo, Sergio R. de Lazaro, Cláudio R.R. Almeida, Carlos A. Paskocimas, Fabiana V. Motta, Mauricio R.D. Bomio.

Category 3

Approval of the version of the manuscript to be published (the names of all authors must be listed):

Ricardo L. Tranquilin, Marisa C. Oliveira, Anderson A. G. Santiago, Laura X. Lovisa, Renan A.P. Ribeiro, Elson Longo, Sergio R. de Lazaro, Cláudio R.R. Almeida, Carlos A. Paskocimas, Fabiana V. Motta, Mauricio R.D. Bomio.

Declaration of competing interest

The authors declare that they have no known competing financial interests or personal relationships that could have appeared to influence the work reported in this paper.

Acknowledgments

The authors thank the following Brazilian research financing institutions for financial support: the National Council for Scientific and Technological Development (CNPq) and the São Paulo Research Foundation FAPESP (2013/07296-2) Graduate Program in Materials Science and Engineering (PPGCEM-UFRN), the Federal University of São Carlos, the State University of Ponta Grossa (Araucária Foundation), and the Coordination for the Improvement of Higher Education Personnel (CAPES), Brazil, Finance Code 001. Marisa C. Oliveira acknowledges the Coordination for the Improvement of Higher Education Personnel (PNPD/CAPES) (88887.319041/2019–00). Anderson A. G. Santiago and Renan A. P. Ribeiro (156176/2018-1) acknowledge financial support from CNPq.

Appendix A. Supplementary data

Supplementary data to this article can be found online at https://doi.org/10.1016/j.jpcs.2020.109790.

References

[1] J. Li, T. Zhang, G. Zhu, Z. Hairong, Up-conversion photoluminescence emissions of $CaMoO_4$:Pr^{3+}/Yb^{3+} powder, J. Rare Earths 35 (2017) 645–651.
[2] A.I. Becerro, M. Allix, M. Laguna, D. González-Mancebo, C. Genevois, A. Caballero, G. Lozano, N.O. Núñez, M. Ocaña, Revealing the substitution mechanism in Eu^{3+}:$CaMoO_4$ and Eu^{3+},Na^{+}:$CaMoO_4$ phosphors, J. Mater. Chem. C 6 (2018) 12830–12840.
[3] D. Gao, Y. Li, X. Lai, Y. Wei, J. Bi, Y. Li, M. Liu, Fabrication and luminescence properties of Dy^{3+} doped $CaMoO_4$ powders, Mater. Chem. Phys. 126 (2011) 391–397.
[4] M. Laguna, N.O. Nuñez, A.I. Becerro, M. Ocaña, Morphology control of uniform $CaMoO_4$ microarchitectures and development of white light emitting phosphors by Ln doping (Ln = Dy^{3+}, Eu^{3+}), CrystEngComm 19 (2017) 1590–1600.
[5] E. Cavalli, P. Boutinaud, R. Mahiou, M. Bettinelli, P. Dorenbos, Luminescence dynamics in Tb^{3+}-doped $CaWO_4$ and $CaMoO_4$ crystals, Inorg. Chem. 49 (2010) 4916–4921.
[6] J. Zhang, T. Zhao, B. Wang, L. Li, L. Zou, S. Gan, PEG-assisted hydrothermal synthesis and photoluminescence of $CdMoO_4$:Tb^{3+} green phosphor, J. Phys. Chem. Solid. 79 (2015) 14–22.
[7] Y. Tan, X. Luo, M. Mao, D. Shu, W. Shan, G. Li, D. Guo, Optimization red emission of $SrMoO_4$: Eu^{3+} via hydro-thermal co-precipitation synthesis using orthogonal experiment, Curr. Appl. Phys. 18 (2018) 1403–1409.
[8] G.M. Gurgel, L.X. Lovisa, L.M. Pereira, F.V. Motta, M.S. Li, E. Longo, C. A. Paskocimas, M.R.D. Bomio, Photoluminescence properties of (Eu, Tb, Tm) co-doped $PbMoO_4$ obtained by sonochemical synthesis, J. Alloys Compd. 700 (2017) 130–137.
[9] A.K. Soni, V.K. Rai, Optical studies in Er^{3+} doped $BaMoO_4$ downconverting phosphor for blue LEDs, AIP Conf. Proc. 1724 (2016), 020002.
[10] X. Yuhang, Z. Xiangyu, Z. Hongbo, Z. Mengjie, M. Shuo, S. Chunhui, J. Shao, Luminescence properties of Eu^{3+} doped $BaMoO_4$ transparent glass ceramics, J. Non-Cryst. Solids 500 (2018) 243–248.
[11] L.S. Cavalcante, V.M. Longo, J.C. Sczancoski, M.A.P. Almeida, A.A. Batista, J. A. Varela, M.O. Orlandi, E. Longo, M.S. Li, Electronic structure, growth mechanism and photoluminescence of $CaWO_4$ crystals, CrystEngComm 14 (2012) 853–868.
[12] G. Wandahl, A.N. Christensen, Neutron powder diffraction profile refinement studies on $CaMoO_4$. A comparison with single-crystal data, Acta Chem. Scand. Ser. A 41 (1987) 358–360.
[13] G. Botelho, I. Nogueira, E. Moraes, E. Longo, Study of structural and optical properties of $CaMoO_4$ nanoparticles synthesized by the microwave-assisted solvothermal method, Mater. Chem. Phys. 183 (2016) 110–120.
[14] V. Marques, L. Cavalcante, J. Sczancoski, A. Alcântara, M.O. Orlandi, E. Moraes, E. Longo, J.A. Varela, M. Siu Li, M. Santos, Effect of different solvent ratios (water/ethylene glycol) on the growth process of $CaMoO_4$ crystals and their optical properties, Cryst. Growth Des. 10 (2010) 4752–4768.

[15] V.B. Mikhailik, H. Kraus, G. Miller, M.S. Mykhaylyk, D. Wahl, Luminescence of $CaWO_4$, $CaMoO_4$, and $ZnWO_4$ scintillating crystals under different excitations, J. Appl. Phys. 97 (2005), 083523.

[16] S. Pan, J. Zhang, J. Pan, G. Ren, J. Lee, H. Kim, Thermal expansion, luminescence, and scintillation properties of $CaMoO_4$ crystals grown by the vertical Bridgman method, J. Cryst. Growth 498 (2018) 56–61.

[17] L. Jiang, Z. Wang, H. Chen, Y. Chen, P. Chen, Z. Xu, Thermal annealing effects on the luminescence and scintillation properties of $CaMoO_4$ single crystal grown by Bridgman method, J. Alloys Compd. 734 (2018) 179–187.

[18] L.B. Barbosa, D.R. Ardila, C. Cusatis, J.P. Andreeta, Growth and characterization of crack-free scheelite calcium molybdate single crystal fiber, J. Cryst. Growth 235 (2002) 327–332.

[19] Y. Zhai, X. Zhao, C. Liu, P. Song, X. Jing, Y. Han, J. Wang, $CaMoO_4:Dy^{3+},Eu^{3+}$ phosphors: microwave synthesis, characterization, tunable luminescence properties and energy transfer mechanism, Optik 164 (2018) 433–442.

[20] J. Xiong, Q. Meng, W. Sun, Luminescent properties and energy transfer mechanism from Tb^{3+} to Eu^{3+} in $CaMoO_4:Tb^{3+},Eu^{3+}$ phosphors, J. Rare Earths 34 (2016) 251–258.

[21] T. Thongtem, S. Kungwankunakorn, B. Kuntalue, A. Phuruangrat, S. Thongtem, Luminescence and absorbance of highly crystalline $CaMoO_4$, $SrMoO_4$, $CaWO_4$ and $SrWO_4$ nanoparticles synthesized by co-precipitation method at room temperature, J. Alloys Compd. 506 (2010) 475–481.

[22] A.A. Ansari, M. Alam, Optical and structural studies of $CaMoO_4$:Sm, $CaMoO_4$:Sm@$CaMoO_4$ and $CaMoO_4$:Sm@$CaMoO_4$@SiO_2 core–shell nanoparticles, J. Lumin. 157 (2015) 257–263.

[23] S.S. Hosseinpour-Mashkani, S.S. Hosseinpour-Mashkani, A. Sobhani-Nasab, Synthesis and characterization of rod-like $CaMoO_4$ nanostructure via free surfactant sonochemical route and its photocatalytic application, J. Mater. Sci. Mater. Electron. 27 (2016) 4351–4355.

[24] S. Li, Q. Meng, S. Lü, W. Sun, Optical properties of Sm^{3+} and Tb^{3+} co-doped $CaMoO_4$ phosphor for temperature sensing, Spectrochim. Acta Part A Mol. Biomol. Spectrosc. 214 (2019) 537–543.

[25] A.A. Ansari, A.K. Parchur, M. Alam, A. Azzeer, Structural and photoluminescence properties of Tb-doped $CaMoO_4$ nanoparticles with sequential surface coatings, Mater. Chem. Phys. 147 (2014) 715–721.

[26] A. Kuzmanoski, V. Pankratov, C. Feldmann, Microwave-assisted ionic-liquid-based synthesis of highly crystalline $CaMoO_4:RE^{3+}$ (RE = Tb, Sm, Eu) and $Y_2Mo_4O_{15}:Eu^{3+}$ nanoparticles, Solid State Sci. 41 (2015) 56–62.

[27] A.A.G. Santiago, E.M. Macedo, F.K.F. Oliveira, F.V. Motta, M.R.D. Bomio, Synthesis and characterization of $BaWO_4:_xTm^{3+},yPr^{3+}$ obtained by ultrasonic spray pyrolysis, J. Mater. Sci. Mater. Electron. 31 (2020) 11599–11608.

[28] A.A.G. Santiago, R.L. Tranquilin, P. Botella, F.J. Manjón, D. Errandonea, C. A. Paskocimas, F.V. Motta, M.R.D. Bomio, Spray pyrolysis synthesis and characterization of $Mg_{1-x}Sr_xMoO_4$ heterostructure with white light emission, J. Alloys Compd. 813 (2020) 152235.

[29] M.-H. Du, Using DFT methods to study activators in optical materials, ECS J. Solid State Sci. 5 (2016) R3007–R3018.

[30] S.K. Gupta, P.S. Ghosh, N. Pathak, R. Tewari, Nature of defects in blue light emitting $CaZrO_3$: spectroscopic and theoretical study, RSC Adv. 5 (2015) 56526–56533.

[31] M.M. Teixeira, R.C. de Oliveira, M.C. Oliveira, R.A. Pontes Ribeiro, S.R. de Lazaro, M.S. Li, A.J. Chiquito, L. Gracia, J. Andrés, E. Longo, Computational chemistry meets experiments for explaining the geometry, electronic structure, and optical properties of $Ca_{10}V_6O_{25}$, Inorg. Chem. 57 (2018) 15489–15499.

[32] M.C. Oliveira, L. Gracia, M. de Assis, I.L.V. Rosa, M.F. do Carmo Gurgel, E. Longo, J. Andrés, Mechanism of photoluminescence in intrinsically disordered $CaZrO_3$ crystals: first principles modeling of the excited electronic states, J. Alloys Compd. 722 (2017) 981.

[33] M.C. Oliveira, R.A.P. Ribeiro, L. Gracia, S.R. de Lazaro, M. de Assis, M. Oliva, I.L. V. Rosa, M.F.d.C. Gurgel, E. Longo, J. Andrés, Experimental and theoretical study of the energetic, morphological, and photoluminescence properties of $CaZrO_3:Eu^{3+}$, CrystEngComm 20 (2018) 5519.

[34] L. Gracia, J. Andrés, V.M. Longo, J.A. Varela, E. Longo, A theoretical study on the photoluminescence of $SrTiO_3$, Chem. Phys. Lett. 493 (2010) 141–146.

[35] V.M. Longo, M. das Graca Sampaio Costa, A. Zirpole Simoes, I.L.V. Rosa, C.O. P. Santos, J. Andres, E. Longo, J.A. Varela, On the photoluminescence behavior of samarium-doped strontium titanate nanostructures under UV light. A structural and electronic understanding, Phys. Chem. Chem. Phys. 12 (2010) 7566–7579.

[36] L. Gracia, V.M. Longo, L.S. Cavalcante, A. Beltrán, W. Avansi, M.S. Li, V. R. Mastelaro, J.A. Varela, E. Longo, J. Andrés, Presence of excited electronic state in $CaWO_4$ crystals provoked by a tetrahedral distortion: an experimental and theoretical investigation, J. Appl. Phys. 110 (2011), 043501.

[37] M.L. Moreira, J. Andrés, L. Gracia, A. Beltrán, L.A. Montoro, J.A. Varela, E. Longo, Quantum mechanical modeling of excited electronic states and their relationship to cathodoluminescence of $BaZrO_3$, J. Appl. Phys. 114 (2013), 043714.

[38] R.A.P. Ribeiro, M.C. Oliveira, M.R.D. Bomio, S.R. de Lazaro, J. Andrés, E. Longo, Connecting the surface structure, morphology and photocatalytic activity of Ag_2O: an in depth and unified theoretical investigation, Appl. Surf. Sci. 509 (2020) 145321.

[39] C.R.R. Almeida, L.X. Lovisa, A.A.G. Santiago, M.S. Li, E. Longo, C.A. Paskocimas, F. V. Motta, M.R.D. Bomio, One-step synthesis of $CaMoO_4$: Eu^{3+} nanospheres by ultrasonic spray pyrolysis, J. Mater. Sci. Mater. Electron. 28 (2017) 16867–16879.

[40] P.N. Medeiros, A.A.G. Santiago, E.A.C. Ferreira, M.S. Li, E. Longo, M.R.D. Bomio, F. V. Motta, Influence Ca-doped $SrIn_2O_4$ powders on photoluminescence property prepared one step by ultrasonic spray pyrolysis, J. Alloys Compd. 747 (2018) 1078–1087.

[41] A.A.G. Santiago, L.X. Lovisa, P.N. Medeiros, M.S. Li, N.L.V. Carreño, E. Longo, C. A. Paskocimas, M.R.D. Bomio, F.V. Motta, Fast and simultaneous doping of $Sr_{0.9-x-y-z}Ca_{0.1}In_2O_4:(xEu^{3+}, yTm^{3+}, zTb^{3+})$ superstructure by ultrasonic spray pyrolysis, Ultrason. Sonochem. 56 (2019) 14–24.

[42] T. Ogihara, T. Kodera, Synthesis of $Li_2Ti_3O_7$ anode materials by ultrasonic spray pyrolysis and their electrochemical properties, Materials 6 (2013) 2285–2294.

[43] P. Majerič, D. Jenko, B. Friedrich, R. Rudolf, Formation mechanisms for gold nanoparticles in a redesigned ultrasonic spray pyrolysis, Adv. Powder Technol. 28 (2017) 876–883.

[44] R. Taziwa, E. Meyer, Fabrication of TiO_2 nanoparticles and thin films by ultrasonic spray pyrolysis: design and optimization, in: M. Samer (Ed.), Pyrolysis, IntechOpen, 2017, https://doi.org/10.5772/67866. London.

[45] A.A.G. Santiago, C.R.R. Almeida, R.L. Tranquilin, R.M. Nascimento, C. A. Paskocimas, E. Longo, F.V. Motta, M.R.D. Bomio, Photoluminescent properties of the $Ba_{1-x}Zn_xMoO_4$ heterostructure obtained by ultrasonic spray pyrolysis, Ceram. Int. 44 (2018) 3775–3786.

[46] R. Dovesi, A. Erba, R. Orlando, C.M. Zicovich-Wilson, B. Civalleri, L. Maschio, M. Rérat, S. Casassa, J. Baima, S. Salustro, B. Kirtman, Quantum-mechanical condensed matter simulations with CRYSTAL, Comput. Mol. Sci. 8 (2018), e1360.

[47] C.T. Lee, W.T. Yang, R.G. Parr, Development of the Colle-Salvetti correlation-energy formula into a functional of the electron density, Phys. Rev. B Condens. Matter 37 (1988) 785–789.

[48] A.D. Becke, Density-functional thermochemistry. III. The role of exact exchange, J. Chem. Phys. 98 (1993) 5648–5652.

[49] C. Gatti, V.R. Saunders, C. Roetti, Crystal field effects on the topological properties of the electron density in molecular crystals: the case of urea, J. Chem. Phys. 101 (1994) 10686–10696.

[50] M. Catti, A. Pavese, V.R. Saunders, Elastic constants and electronic structure of fluorite (CaF_2): an ab initio Hartree-Fock study, J. Phys. Condens. Matter 3 (1991) 4151–4164.

[51] F. Corà, A. Patel, N.M. Harrison, C. Roetti, C. Richard A. Catlow, An ab initio Hartree–Fock study of α-MoO_3, J. Mater. Chem. 7 (1997) 959–967.

[52] K.E. El-Kelany, C. Ravoux, J.K. Desmarais, P. Cortona, Y. Pan, J.S. Tse, A. Erba, Spin localization, magnetic ordering, and electronic properties of strongly correlated Ln_2O_3 sesquioxides (Ln=La, Ce, Pr, Nd), Phys. Rev. B 97 (2018) 245118.

[53] H.J. Monkhorst, J.D. Pack, Special points for Brillouin-zone integrations, Phys. Rev. B 13 (1976) 5188.

[54] A.K. Parchur, R.S. Ningthoujam, Preparation and structure refinement of Eu^{3+} doped $CaMoO_4$ nanoparticles, Dalton Trans. 40 (2011) 7590–7594.

[55] V.M. Longo, A.T.d. Figueiredo, A.B. Campos, J.W.M. Espinosa, A.C. Hernandes, C. A. Taft, J.R. Sambrano, J.A. Varela, E. Longo, Different origins of green-light photoluminescence emission in structurally ordered and disordered powders of calcium molybdate, J. Phys. Chem. 112 (2008) 8920–8928.

[56] R. Shannon, Revised effective ionic radii and systematic studies of interatomic distances in halides and chalcogenides, Acta Crystallogr. A 32 (1976) 751–767.

[57] W.M. Haynes (Ed.), CRC Handbook of Chemistry and Physics, 95th ed., CRC Press, Boca Raton, 2014.

[58] G.L. Messing, S.-C. Zhang, G.V. Jayanthi, Ceramic powder synthesis by spray pyrolysis, J. Am. Ceram. Soc. 76 (1993) 2707–2726.

[59] J.F. Scott, Lattice perturbations in $CaWO_4$ and $CaMoO_4$, J. Chem. Phys. 48 (1968) 874–876.

[60] W. Gao, Z. Li, N.M. Sammes, An Introduction to Electronic Materials for Engineers, World Scientific, Singapore, 2011.

[61] D.L. Wood, J. Tauc, Weak absorption tails in amorphous semiconductors, Phys. Rev. B 5 (1972) 3144–3151.

[62] E. Burstein, Anomalous optical absorption limit in InSb, Phys. Rev. 93 (1954) 632–633.

[63] R.L. Tranquilin, L.X. Lovisa, C.R.R. Almeida, C.A. Paskocimas, M.S. Li, M. C. Oliveira, L. Gracia, J. Andres, E. Longo, F.V. Motta, M.R.D. Bomio, Understanding the white-emitting $CaMoO_4$ co-doped Eu^{3+}, Tb^{3+}, and Tm^{3+} phosphor through experiment and computation, J. Phys. Chem. C 123 (2019) 18536–18550.

[64] V. Panchal, N. Garg, H.K. Poswal, D. Errandonea, P. Rodríguez-Hernández, A. Muñoz, E. Cavalli, High-pressure behavior of $CaMoO_4$, Phys. Rev. Mater. 1 (2017), 043605.

[65] P. Dorenbos, A.H. Krumpel, E. van der Kolk, P. Boutinaud, M. Bettinelli, E. Cavalli, Lanthanide level location in transition metal complex compounds, Opt. Mater. 32 (2010) 1681–1685.

[66] P. Dorenbos, The $4f^n \leftrightarrow 4f^{n-1}5d$ transitions of the trivalent lanthanides in halogenides and chalcogenides, J. Lumin. 91 (2000) 91–106.

[67] P. Dorenbos, Lanthanide charge transfer energies and related luminescence, charge carrier trapping, and redox phenomena, J. Alloys Compd. 488 (2009) 568–573.

[68] P. Boutinaud, P. Putaj, R. Mahiou, E. Cavalli, A. Speghini, M. Bettinelli, Quenching of lanthanide emission by intervalence charge transfer in crystals containing closed shell transition metal ions, Spectrosc. Lett. 40 (2007) 209–220.

[69] P. Dorenbos, Systematic behaviour in trivalent lanthanide charge transfer energies, J. Phys. Condens. Matter 15 (2003) 8417–8434.

[70] P. Boutinaud, E. Cavalli, M. Bettinelli, Emission quenching induced by intervalence charge transfer in Pr^{3+}- or Tb^{3+}-doped $YNbO_4$ and $CaNb_2O_6$, J. Phys. Condens. Matter 19 (2007) 386230.

[71] P. Dorenbos, Crystal field splitting of lanthanide $4f^{n-1}5d$-levels in inorganic compounds, J. Alloys Compd. 341 (2002) 156–159.

[72] I. Kebaïli, M. Dammak, E. Cavalli, M. Bettinelli, Energy levels and crystal-field analysis of Tm^{3+} in $YAl_3(BO_3)_4$ crystals, J. Lumin. 131 (2011), 2010–2015.

[73] E. Cavalli, F. Angiuli, I. Kebaïli, M. Dammak, P. Boutinaud, M. Bettinelli, Luminescence dynamics of $YAl_3(BO_3)_4:Sm^{3+}$ crystals, J. Lumin. 143 (2013) 562–565.
[74] N. Ben Amar, T. Koubaa, M.A. Hassairi, I. Kbaïli, M. Dammak, Optical spectroscopy of Eu^{3+} ions doped in $YAl_3(BO_3)_4$ crystal, J. Lumin. 160 (2015) 95–100.
[75] S. Mahlik, M. Behrendt, M. Grinberg, E. Cavalli, M. Bettinelli, High pressure luminescence spectra of $CaMoO_4:Ln^{3+}$(Ln = Pr, Tb), J. Phys. Condens. Matter 25 (2013) 105502.
[76] X. Zhou, X. Yang, T. Xiao, K. Zhou, T. Chen, H. Yan, Z. Wang, Luminescence properties and energy transfer of host sensitized $CaMoO_4:Tb^{3+}$ green phosphors, J. Rare Earths 31 (2013) 655–659.
[77] S. Shi, X. Liu, J. Gao, J. Zhou, Spectroscopic properties and intense red-light emission of (Ca, Eu, M)WO_4 (M=Mg, Zn, Li), Spectrochim, Acta Part A Mol. Biomol. Spectrosc. 69 (2008) 396–399.
[78] T. Selvalakshmi, S. Sellaiyan, A. Uedono, A. Chandra Bose, Investigation of defect related photoluminescence property of multicolour emitting $Gd_2O_3:Dy^{3+}$ phosphor, RSC Adv. 4 (2014) 34257–34266.
[79] Y. Xie, Z. Ma, L. Liu, Y. Su, H. Zhao, Y. Liu, Z. Zhang, H. Duan, J. Li, E. Xie, Oxygen defects-modulated green photoluminescence of Tb-doped ZrO_2 nanofibers, Appl. Phys. Lett. 97 (2010) 141916.
[80] K.P.F. Siqueira, A.P. Carmo, M.J.V. Bell, A. Dias, Influence of crystalline structure on the luminescence properties of terbium orthotantalates, J. Lumin. 138 (2013) 133–137.
[81] A.K. Parchur, A.I. Prasad, A.A. Ansari, S.B. Rai, R.S. Ningthoujam, Luminescence properties of Tb^{3+}-doped $CaMoO_4$ nanoparticles: annealing effect, polar medium dispersible, polymer film and core–shell formation, Dalton Trans. 41 (2012) 11032–11045.
[82] S.W. Park, B.K. Moon, J.H. Jeong, J.S. Bae, J.H. Kim, Crystal structure, electronic structure, and photoluminescent properties of $SrMoO_4:Tb^{3+}$ phosphors, Mater. Res. Bull. 70 (2015) 403–411.
[83] J. Zhang, G.M. Cai, G.X. Zhang, Z.P. Jin, Insight into crystal structure and Eu/Tb doped luminescence property of a new phosphate, J. Alloys Compd. 762 (2018) 444–455.
[84] L.X. Lovisa, M.C. Oliveira, J. Andrés, L. Gracia, M.S. Li, E. Longo, R.L. Tranquilin, C.A. Paskocimas, M.R.D. Bomio, F.V. Motta, Structure, morphology and photoluminescence emissions of $ZnMoO_4$: RE^{3+}=Tb^{3+} - Tm^{3+} - X Eu^{3+} (x = 1, 1.5, 2, 2.5 and 3 mol%) particles obtained by the sonochemical method, J. Alloys Compd. 750 (2018) 55.
[85] S. Li, Q. Meng, S. Lü, W. Sun, Study on optical temperature sensing properties of Tb^{3+}, Eu^{3+} co-doped $CaMoO_4$ phosphor, J. Lumin. 200 (2018) 103–110.
[86] J. Yu, K. Huang, L. Yuan, S. Feng, Hydrothermal syntheses and photoluminescence properties of rare-earth tungstate as near ultraviolet type red phosphors, New J. Chem. 38 (2014) 1441–1445.
[87] P. Jena, S.K. Gupta, V. Natarajan, M. Sahu, N. Satyanarayana, M. Venkateswarlu, Structural characterization and photoluminescence properties of sol–gel derived nanocrystalline $BaMoO_4:Dy^{3+}$, J. Lumin. 158 (2015) 203–210.
[88] G. Blasse, Energy transfer between inequivalent Eu^{2+} ions, J. Solid State Chem. 62 (1986) 207.
[89] E.F. Schubert, Light Emitting Diodes, Cambridge University Press, Cambridge, 2003.
[90] A.R. Robertson, Computation of correlated color temperature and distribution temperature, J. Opt. Soc. Am. 58 (1968) 1528–1535.
[91] L.X. Lovisa, J. Andrés, L. Gracia, M.S. Li, C.A. Paskocimas, M.R.D. Bomio, V. D. Araujo, E. Longo, F.V. Motta, Photoluminescent properties of ZrO_2: Tm^{3+}, Tb^{3+}, Eu^{3+} powders—a combined experimental and theoretical study, J. Alloys Compd. 695 (2017) 3094–3103.